



Comparison of force measurement techniques in a short duration hypersonic facility

Andrew Hyslop¹ · Luke J. Doherty¹ · Matthew McGilvray¹

Received: 20 August 2023 / Revised: 18 December 2023 / Accepted: 2 January 2024 / Published online: 3 February 2024
© The Author(s) 2024

Abstract

Force measurement experiments have been conducted within the University of Oxford's High Density Tunnel with a 7° half-angle cone. The purpose of the study was to provide a direct comparison between two independent force techniques in the same facility at the same free-stream conditions to provide a quantitative and qualitative discussion of the advantages and disadvantages of both techniques. The first force measurement technique used a conventional 4-axis sting-mounted force balance which was calibrated both statically and through the stress wave deconvolution method, whilst the second technique used the less established static free-flight methodology. Experiments were conducted at a Mach 5 test condition which provided sufficient dynamic pressure to generate aerodynamic forces suitable for the measurement range of the force balance. Results for lift, drag and pitching moment coefficients were obtained over a range of angles of attack and compared with predictions from a hypersonic panel method code. Agreement between the independent force techniques and numerical data sets was good over the range of angles of attack. Maximum uncertainties were shown to be 38.46 ± 0.56 N and 22.52 ± 0.44 N for free-flight in lift and drag, respectively, and 38.74 ± 1.59 N and 22.13 ± 1.27 N for the dynamically calibrated force balance which demonstrates the superiority of free-flight.

1 Introduction

The ability to obtain high quality force measurement data with low uncertainties is vital when developing new vehicles in all flight regimes, subsonic to hypersonic. For subsonic to supersonic flows, the methodology of force measurements is well established as blow-down facilities can replicate flight conditions for long, steady test times (minutes to hours) which allows for strain gauge force balances to be used. In the field of hypersonics, facilities that are able to replicate scaled flight Reynolds numbers, such as Ludwig tubes, produce very short duration flow in the order of milliseconds

to tens of milliseconds. Due to the limited test time available to experimenters, the temporal response of models and supporting structures must be considered which can make it difficult to obtain high quality force data. Furthermore, numerical nose-to-tail simulations of hypersonic vehicles are difficult and computationally expensive as phenomena such as boundary layer transition are challenging to predict (Wuillbercq et al. 2014; Stetson 1992) which motivates efforts to obtain accurate force data from experiments.

There have been two major approaches over the years to obtain high quality force data in the area of hypersonics that are discussed in detail in Bernstein and Pankhurst (Bernstein and Pankhurst 1975), the first of which is to use a sting-mounted force balance. This is the most common method of determining aerodynamic forces and moment in wind tunnels facilities, particularly in the subsonic regime. In its most simplistic form, a strain gauge load cell is located within the supporting structure and used to directly measure the forces at the point of equilibrium providing aerodynamic data which is representative of the full-scale vehicle. This can range from single-component drag measurements to six-component force and moment measurements. Frequently, the attitude of the model will be controlled by the operator between tests to characterise the model at a range of

Luke J. Doherty and Matthew McGilvray have contributed equally to this work.

✉ Andrew Hyslop
andrew.hyslop@eng.ox.ac.uk

Luke J. Doherty
luke.doherty@eng.ox.ac.uk

Matthew McGilvray
matthew.mcgilvray@eng.ox.ac.uk

¹ Department of Engineering Science, University of Oxford, Osney Mead, Oxford, Oxfordshire OX2 0ES, UK

orientations. This methodology works well for blow-down facilities or hypersonic facilities with sufficient test time (Calloway 1981; Milhous et al. 1971). However, in short duration facilities with test times in the order of milliseconds to tens of milliseconds, the impulsive nature of the facilities results in stress waves within the model mounting structure that do not reach equilibrium within the test time and hence makes it difficult to obtain quasi-static aerodynamic forces. To overcome these issues, the stress wave technique was developed by Sanderson and Simmons (Sanderson and Simmons 1991) resolving the drag force acting on an axisymmetric body in flow duration of 1 ms. This technique requires a dynamic calibration of the model force balance structure to determine the system impulse response function. Knowledge of the impulse response function of the model and sufficient characterisation of the stress wave patterns allows the experimenter to deconvolve the measured strain signals to determine the net aerodynamic load. The calibration is achieved through a series of instrumented impulse hammer hits as described by Mee (2003) for a single-component balance and Doherty et al. (2015) for a three-component balance.

Another well documented issue with force balance measurements is the interference of the sting that can result in undesirable effects in drag (Pick 1971). The interaction between the sting-model supporting structure can influence the pressure field around the test model, resulting in a larger measured aerodynamic force. Therefore, care must be taken with the model mounting structure to prevent this from occurring.

The other approach to force measurement experiments in hypersonic facilities is known as the free-flight technique. This removes the sting and allows the model to move freely in 6 degrees of freedom. A typical methodology of a free-flight test in short duration facilities is as follows: the model is released prior to arrival of the test flow, the flow is initiated over the model which moves as it would in flight. An alternative method is to support the model with thin filaments which are broken during flow initialisation. As the model is not constrained, non-intrusive methods of measuring accelerations, rather than forces, are required. Free-flight wind tunnel experiments are discussed at length in Dayman (1966) and later in Bernstein and Pankhurst (1975). These very early efforts were hampered by difficulty in achieving high frame rate images and lack of miniature electronics. With the miniaturisation of IMU's driven by mobile phone technology, and the availability of high-resolution cameras with high frame rates, there has been a strong resurgence of the technique over the last decade and it is now widely used in short duration facilities around the world including for multi-body separation problems (Leiser et al. 2022; Grossir et al. 2020; Park and Park 2020) and the measurement of static aerodynamic force coefficients of high-inertia models in shock tunnels (Tanno and Tanno 2021; Tanno et al.

2014). Low inertia models in free-flight have also been used to measure aerodynamic forces as demonstrated by Kennell et al. (2016, 2017) with ESA's HEXAFly INT EFTV geometry, McQuellin et al. (2020) with an axisymmetric flyer and sustainer, and Hyslop et al. (2021) for Reaction Engines' Skylon spaceplane. For these experiments, low inertia models were used which allowed the model to freely pitch over a wide range of angles of attack during a test and hence providing large sweeps of aerodynamic coefficient data in a single run. With the large amounts of pitching during the test, the aerodynamic coefficients will include some dynamic influence in the measurement (Hyslop 2023). This paper presents a direct comparison of force measurement of two independent techniques in the University of Oxford High Density Tunnel (HDT) applied to a 7° half-angle cone. Both free-flight, previously used by Hyslop et al. (2022), and force balance with stress wave deconvolution are used to determine the aerodynamic coefficients at a Mach 5 test condition. The advantages and disadvantages of both techniques will be discussed in detail in this paper.

2 Experimental facility

2.1 University of Oxford High Density Tunnel

The experiments were conducted in the University of Oxford High Density Tunnel (HDT), located within the Oxford Thermofluids Institute. Whilst the facility has multiple modes of operation, for these tests it was operated as a heated Ludwieg tube which provides approximately 50 ms of steady flow duration during which force measurements are taken. The facility was fitted with a Mach 5 contoured nozzle of exit diameter of 351 mm that produces a core flow of 280 mm at nozzle exit. The facility is typically operated at total pressures up to 60 bar but is rated for fill pressures of 275 bar. For further details on the HDT operation and measurement of free-stream conditions, see (McGilvray et al. 2015) and Wylie et al. (2018). Figure 1 shows a schematic of the Oxford HDT and Fig. 2 shows typical total pressure and temperature traces at the test conditions used in these experiments. Only the first plateau was used as the test time in which forces were measured, as after this time, the free-flight model is no longer in the core flow. For the total temperature trace, a spike can be seen in the data before the test time which is due to the unsteady filling of the tunnel plenum prior to flow passing through the nozzle. It has settled before the test time so a constant Reynolds number can be assumed in the subsequent plateaus.

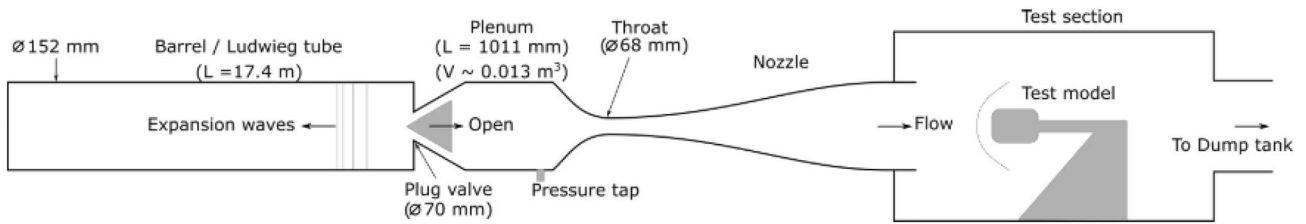


Fig. 1 Schematic of the University of Oxford HDT (adapted from D Hillyer et al. (2022))

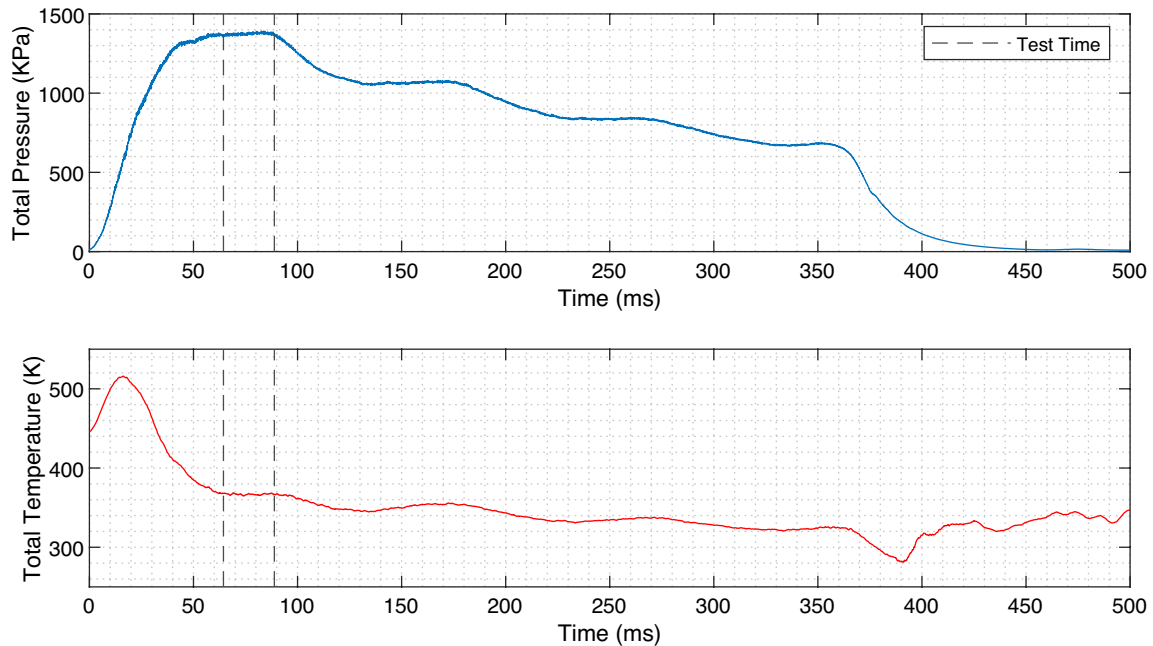


Fig. 2 Example total pressure and temperature traces for the HDT

2.2 Test conditions

For this work, a test condition was chosen that provided sufficient dynamic pressure such that the aerodynamic forces acting on the model were suitably in the range of the 0.7 inch force balance discussed in Sect. 4. The condition used was a Mach 5 flow with a total pressure of 13.8 bar. The free-stream conditions were determined using an instrumented twin probe during the force balance experiments. This consisted of a Pitot probe, which allowed for the measurement of free-stream Mach number using the ratio of pitot to stagnation pressure, and an aspirated thermocouple allowing for the measurement of free-stream total temperature. Dynamic viscosity was calculated using Keyes’ Law (Keyes 1951) and static pressure and temperature through isentropic relations with an assumed ratio of specific heats of 1.4.

Prior to the force experiments, the diameter of the core flow was measured using a rake instrumented with pressure sensors. At nozzle exit, the core flow was determined to be

Table 1 HDT conditions during test time

	HDT test flow
<i>Measured free-stream properties</i>	
Total pressure (kPa)	1375 ± 7.2
Pitot pressure (kPa)	88.3 ± 0.7
Total temperature (K)	369 ± 15
<i>Calculated free-stream properties</i>	
Mach number	4.95 ± 0.01
Velocity (ms ⁻¹)	785 ± 16
Density (kg m ⁻³)	0.153 ± 0.007
Static pressure (Pa)	2759 ± 41
Static temperature (K)	62.7 ± 2.6
Dynamic viscosity (μPas)	4.50 ± 0.18
Dynamic pressure (kPa)	47.3 ± 0.7
Unit Reynolds number (10 ⁶ m ⁻¹)	26.8 ± 1.7

280 mm reducing to 240 mm at 300 mm downstream. A full summary of the test conditions is given in Table 1. Flow angularity was predicted using Eilmer4 CFD (Gibbons et al. 2023) to remain within $\pm 0.12^\circ$ within the core flow.

3 Static free-flight

The methodology used for these experiments uses the same set up as in Hyslop et al. (2022) and therefore only an overall summary is provided. A free-flight experiment is conducted in the HDT as follows, the model is released from an electromagnet and allowed to fall freely. When the model has reached a suitable height relative to the core flow of the tunnel, the tunnel fires and the model is allowed to move freely in 6 degrees of freedom. As the model is not restrained, non-intrusive methods of measuring the model's kinematics are required. For this work, linear and angular displacements are measured directly using image tracking and linear accelerations and angular velocities are measured via an onboard inertial measurement unit (IMU). To achieve the static free-flight condition, where the amount of pitching exhibited by the model is minimised, the model is ballasted so that the centre of gravity (CoG) location is as close to the centre of pressure (CoP) as possible, hence minimising the aerodynamic pitching moment.

3.1 Infrastructure

The test infrastructure used to conduct free-flight experiments in the HDT is shown in Fig. 3 and consists of protective nets, foam padding and a drop mechanism. The drop mechanism consists of a 25 mm electromagnet that is connected to a 50 mm SMC pneumatic actuator that retracts to

remove the electromagnet from the core flow after model release to prevent any undesirable shocks from the flow field. The mechanism is controlled by a bespoke electrical unit that upon receiving a TTL pulse, de-energises the electromagnet and powers two solenoids to retract the actuator. The electromagnet is contained within a 3D printed holder that fits conformal to the model surface, allowing for repeatable alignment in roll and axial position. Different holders were printed to allow the initial angle of attack of the model to be set at 0, 3 and 6°. A steel rod is inserted into the holder prior to a test to fix the model yaw.

To protect the model after a test, a catcher mechanism consisting of two aluminium rings interwoven with Dyneema string was implemented. The upstream ring was held at a 30° inclination with the purpose of deflecting the model to the tunnel floor which is padded with foam providing a soft impact surface. The second downstream ring is a redundancy that prevents the model exiting the test section into the dump tank where it would be difficult to retrieve.

3.2 Model

The experimental model was a 7° half-angle cone of length 250 mm with a nose bluntness of 1.25 mm in radius. The model was manufactured in two halves so that it was modular for ease of instrumentation and ballasting. The main body of the cone was made from steel and the nose tips aluminium. An exploded photo of the cone model is shown in Fig. 4.

The most important aspect of this model was the ability to accurately ballast and locate the position of the CoG of the model so that the model does not pitch during the test, thereby creating the static condition. The model was ballasted using tungsten disks that could have their axial

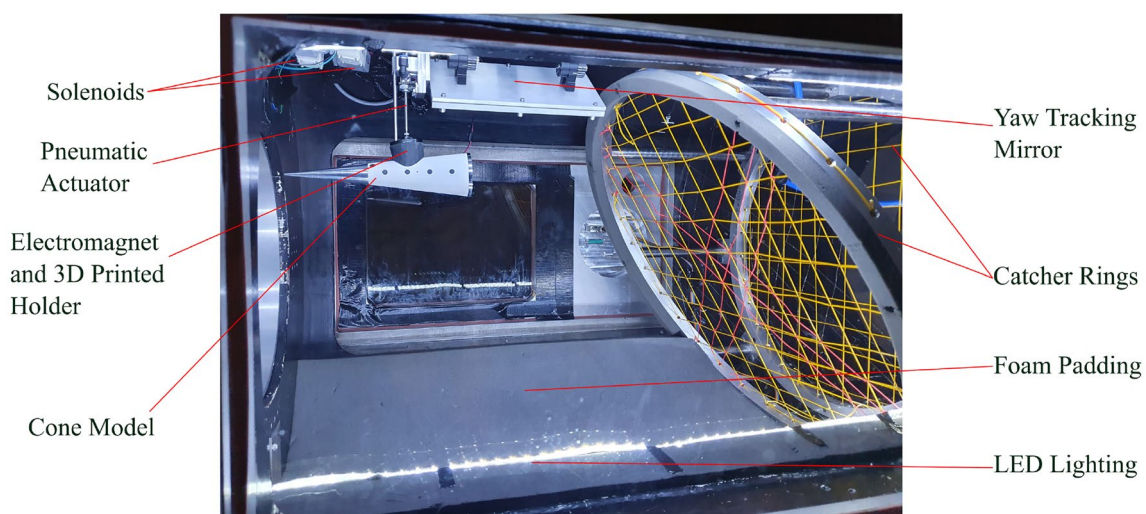


Fig. 3 Free-flight drop mechanism and catcher rings in the HDT test section

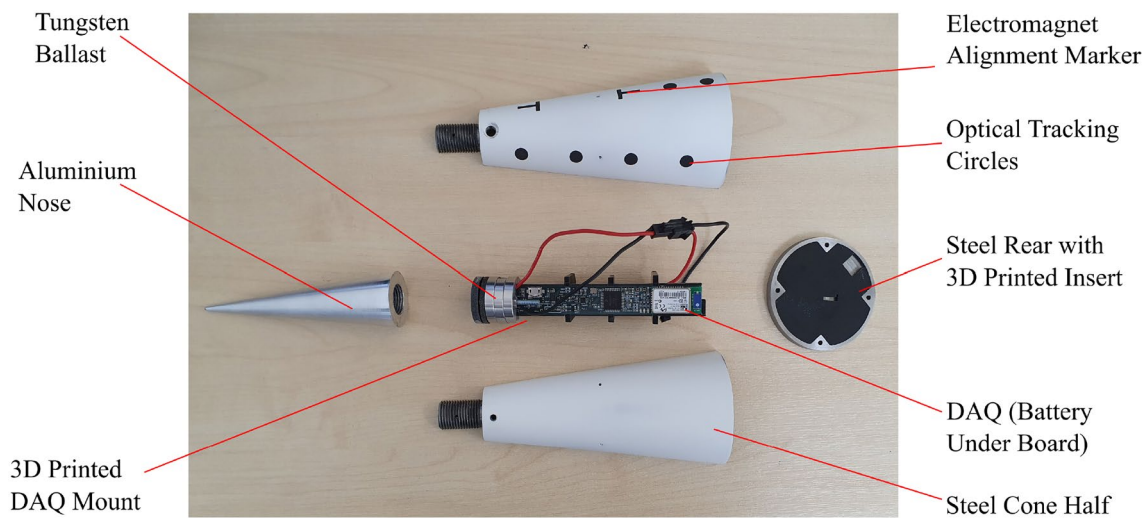


Fig. 4 Constituent components of the free-flight 7° cone model

Table 2 Model inertial and geometric properties

Length (mm)	250 ± 0.2
Cone half-angle (°)	7 ± 0.03
Nominal nose radius (mm)	1.25 ± 0.1
Base area (m ²)	3.2 × 10 ⁻³ ± 0.01
Centre of gravity (mm)	84.2 ± 0.1
Mass (g)	671.261 ± 0.001
Moment of inertia (kgm ²)	2.17 × 10 ⁻³

position adjusted through the use of threaded steel rods. The tungsten ballast allowed for the CoG to be shifted between the ranges of 80.1–85.7 mm from the cone base. The CoP location was predicted to be 84.2 mm (from the cone base) prior to testing using tangent-cone theory (stagnation pressure coefficient of 1.81) and the CoG was set to this position for the experiments. The CoG was measured using a moment balance, whereby the model was suspended using two strings. The tension in the upstream string was measured using a load cell. This setup allowed the CoG to be determined to ± 0.1 mm. The inertial properties of the model are shown in Table 2.

Located internally within the model was an onboard DAQ that consisted of an IMU containing a 3 axis accelerometer (± 16 g) and gyroscope (± 2000 deg/s) which were designed and built by UNSW Canberra. The IMU had a sample rate of 8 kHz and could be armed via an external terminal through Bluetooth. Triggering of the instrument was achieved by detection of sustained free-fall upon model release. On the exterior of the model, a laser-cut stencil was designed to airbrush black dots for the purpose of image tracking. Two “T” shapes were also painted on the model to locate the release point of the

model for the desired CoG location to minimise pitching during model free-fall.

3.3 Data reduction

Aerodynamic force coefficients were derived using two independent methodologies. Both methods ultimately measure the model’s acceleration to determine the instantaneous forces acting on the model during the test time using the model’s mass and moment of inertia (Table 2). The forces are then non-dimensionalised by the free-stream dynamic pressure (Table 1) and a reference area, which for this model was taken to be the cone base area ($S = 3.2 \times 10^{-3} \text{ m}^2$). The reference length used in the calculation of pitching moment was the model length. The aerodynamic coefficients were calculated as follows:

$$C_L = \frac{m(\ddot{z} - g)}{\bar{q}S}, \quad C_D = \frac{m\ddot{x}}{\bar{q}S}, \quad C_M = \frac{I_{yy}\ddot{\theta}}{\bar{q}Sc} \quad (1)$$

where C_L is the lift coefficient, C_D is the drag coefficient, C_M is the pitching moment coefficient, \ddot{z} and \ddot{x} are linear accelerations, $\ddot{\theta}$ is the pitch angular acceleration, \bar{q} is the dynamic pressure, m is the model’s mass, g is the acceleration due to gravity, I_{yy} is the model’s pitch moment of inertia, S is a reference area and c is a reference length.

3.3.1 Inertial measurement unit

When using inertial measurement units that are free to move in space, it is important that co-ordinate systems of interest are well defined so that accelerations and angular placement are referenced to the correct frame before calculating the forces acting on the body. There are two frames of references

used in free-flight experiments—the first is known as the Inertial/Earth co-ordinate system which is defined as having the +z axis towards the ground, +x axis pointing upstream towards the facility nozzle and the +y axis orthogonal to both to form a right-hand co-ordinate system. This frame of reference is what all global force coefficients are defined relative to. The second co-ordinate system is referred to as the body frame of reference. This is defined relative to the model as +x towards the nose of the vehicle, +z towards the bottom of the vehicle with +y completing the orthogonal system. The IMU located on the model measures accelerations and angular velocities in the body frame of reference and hence during a test, this frame of reference is moving relative to the Inertial frame.

To process the raw IMU data, the data are filtered with a 6th order low pass Butterworth filter with a cut off frequency of 500 Hz to remove high frequency noise. The body angular rates are then transformed to Euler angular rates, using Eq. 2, allowing the Euler angles to be determined via numerical integration of Euler-rates. Using the Euler angles, the linear accelerations measured by the IMU are transformed to the inertial frame of reference according to Eq. 3. A gyroscope is unable to measure its attitude relative to the free-stream and so initial conditions must be set before the angular velocities are differentiated. For this work, the initial angle of attack is calculated using image tracking of the external edge of the cone. Finally the aerodynamic coefficients can be obtained using Eq. 1.

The rotation matrix for the angular rates and accelerations are as follows:

$$\begin{bmatrix} \dot{\phi} \\ \dot{\theta} \\ \dot{\psi} \end{bmatrix} = \begin{bmatrix} 1 & s(\phi)t(\theta) & c(\phi)t(\theta) \\ 0 & c(\phi) & -s(\phi) \\ 0 & \frac{s(\phi)}{c(\theta)} & \frac{c(\phi)}{c(\theta)} \end{bmatrix} \begin{bmatrix} p \\ q \\ r \end{bmatrix} \tag{2}$$

$$\begin{bmatrix} \ddot{X} \\ \ddot{Y} \\ \ddot{Z} \end{bmatrix}_E = \begin{bmatrix} c(\psi)c(\theta) & c(\psi)s(\phi)s(\theta) - c(\phi)s(\psi) & s(\phi)s(\psi) + c(\phi)c(\psi)s(\theta) \\ c(\theta)s(\psi) & c(\phi)c(\psi) + s(\phi)s(\psi)s(\theta) & c(\phi)s(\psi)s(\theta) - c(\psi)s(\phi) \\ -s(\theta) & c(\theta)s(\phi) & c(\phi)c(\theta) \end{bmatrix} \begin{bmatrix} \ddot{X} \\ \ddot{Y} \\ \ddot{Z} \end{bmatrix}_B \tag{3}$$

where *c*, *s* and *t* are cosine, sine and tangent functions; respectively, *p*, *q* and *r* are body roll, pitch and yaw rates, respectively, and ϕ , θ and ψ are Euler angles.

3.3.2 Image tracking

Optical tracking was used for free-flight to directly measure the model’s displacement about the centre of gravity and track the angle of attack with respect to the test time. After determining the displacement history of the model, the data can be differentiated twice to obtain the accelerations acting on the model and hence forces. The model was imaged using

a Photron FASTCAM AX200 high-speed camera set to a frame rate of 6400 fps with 1024 × 1024 pixel resolution at a focal length of 50 mm at f2.8. The camera faced directly through the test section windows, imaging the longitudinal plane of motion of the model. To fully capture the free-fall of the model, a pre-trigger of 500 frames was used and a total of 2180 frames recorded, activated by a TTL pulse from the facility prior to the test. Six 1000 lumen torches were used to illuminate the model, providing adequate spacial uniformity of light. The spatial uniformity and distortion of the lens was corrected in post-processing using the MATLAB camera calibrator app through the use of a uniform grid inserted into the tunnel.

The method used to measure the model’s longitudinal displacement in free-flight consisted of tracking black circles painted on a white background, to provide high contrast between the circle and the model body, as seen in Fig. 3. The circles were painted with a locational accuracy of ± 0.1 mm on the model. As seen in the Figure, there are four circles painted on the model but only two are required for the algorithm to locate the position of the centre of gravity. This added redundancy exists in case one of the circles is damaged. The methodology for image tracking is the same as in the work of Hyslop et al. (2021) but the steps can be summarised as follows:

1. Apply Gaussian filter to image and subtract from original (High pass filter).
2. Apply Canny filter to image so that only pixels detected as an edge are shown (Canny 1986).
3. Apply Hough transform to find circles in the image after narrowing the search radius (Hough 1962).
4. Detect pixels in the proximity of the circle located by the Hough transform.
5. Use sub-pixel detection on the original image, at the location pixels were detected. Sub-pixel methodology set out in von Gioi and Randall (2017).
6. Fit a circle to the pixels using linear regression as set out in Laurence and Hornung (2009) and use this equation to find the centre point of the circle.

The CoG of the model is measured with a moment balance prior to an experiment (to an accuracy of ± 0.1 mm) and the locations of the circles painted on the model are known (also to an accuracy of ± 0.1 mm). Therefore, once the centre points of the two circles has been detected, a line can be fitted between the two points and linear interpolation can be used to find the CoG. This process is repeated for each frame giving a time history of centre of gravity displacement and angle of attack. As the distance between the centre points is also a known quantity, the scale of the image can be calculated. For this optical setup, the scaling factor was 0.69 mm/pixel. Figure 5 presents a composite image of a

typical free-flight experiment with the image tracking algorithm detection points overlaid as well as the extent of the nozzle core flow.

In theory, angle of attack can be calculated using the circles on the model; however, it has been found that this methodology is very sensitive to perspective and model yaw. This could be overcome with a second optical camera tracking on the yaw plane. However, this is challenging to implement within the current HDT test section due to lack of optical access. Angle of attack is detected by finding the relative angle between the edge of the cone and the horizontal. As the model was painted white, there is strong contrast between the background of the image and the cone which allows for the edge to be detected with a Canny filter followed by sub-pixel detection to find the true edge. Fitting these points with a straight line and calculating the gradient allows for the angle of attack to be determined. The accuracy of the algorithm was analysed by calculating the position of centre of gravity for 1000 frames where the model was held stationary within the test section. The standard deviation of centre of gravity position for this test was calculated to be $4\ \mu\text{m}$. The pixel resolution was $0.67\ \text{mm/pixel}$, and the radius of the detected circles was approximately 5 pixels out of a frame size of 1024×1024 . These results indicate that the image tracking algorithm can reliably detect the CoG of the model with high accuracy. This analysis does not take into account errors which result from misalignment of the optical equipment but gives an approximation of the uncertainty associated with the numerical algorithm.

To determine the aerodynamic coefficients, the displacement data are differentiated twice to give the accelerations

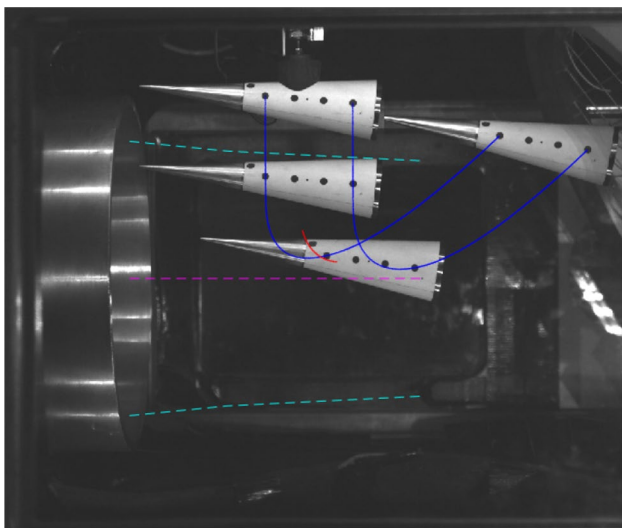


Fig. 5 Montage photo of image processing (Blue—detected circle centre points, Red—calculated centre of gravity, shown for test time, cyan lines show core flow location as acquired by a pitot survey)

and hence aerodynamic coefficients using Eq. 1. The intermediate velocity data required numerical smoothing using a Gaussian filter before being differentiated into accelerations. The maximum filter window for this process corresponds to 15 ms which is sufficiently less than the facility test time (50 ms, see Fig. 2) and allows steady aerodynamic forces to be determined as the static free-flight methodology reduces the pitching of the model, resulting in near constant forces.

3.4 Comparison of image tracking and IMU

Figure 6 shows a comparison between the model kinematics for a single free-flight test at 6° angle of attack between the image tracking and IMU. The image tracking measures displacements directly so the accelerations are determined from differentiation and the IMU measures accelerations directly so the displacements are determined through integration. For the plots shown in Fig. 6, the agreement between the two independent methodologies is excellent, demonstrating the either method can reliably be used to accurately measure static aerodynamic coefficients in free-flight experiments.

The IMU shows small vibrations superimposed on the accelerometer signals which is the result of internal vibrations passing through the mounting structure during the free-flight test. The agreement between the velocity and displacement data on both axes is very good for the entire duration of the experiment. Angle of attack agreement is good; however, some pitching motion can be seen to be exerted on the model when released from the electromagnet. This is challenging to limit as the release point of the mechanism must be exactly above the centre of gravity to prevent pitching motion during free-fall. It can be seen that the angle of attack remains within $5.9 \pm 0.2^\circ$ during the test time.

4 Force balance

This section will discuss the methodology and data reduction used to obtain aerodynamic force coefficients from a 0.7 inch 4-axis force balance used in the HDT with the 7° half-angle cone as the test model. Two conical models were used for the force balance experiments, a steel cone that could be instrumented with pressure transducers to allow alignment with the free-stream, and a nylon cone designed to optimise the stress wave transmission for force measurement.

4.1 0.7 inch force balance

The 0.7 inch force balance is an internal balance that can measure forces on 3 orthogonal axes (axial, normal and side) and the pitching moment. The rated forces and moments

Fig. 6 Comparison of image tracking and IMU data from free-flight shot 2240

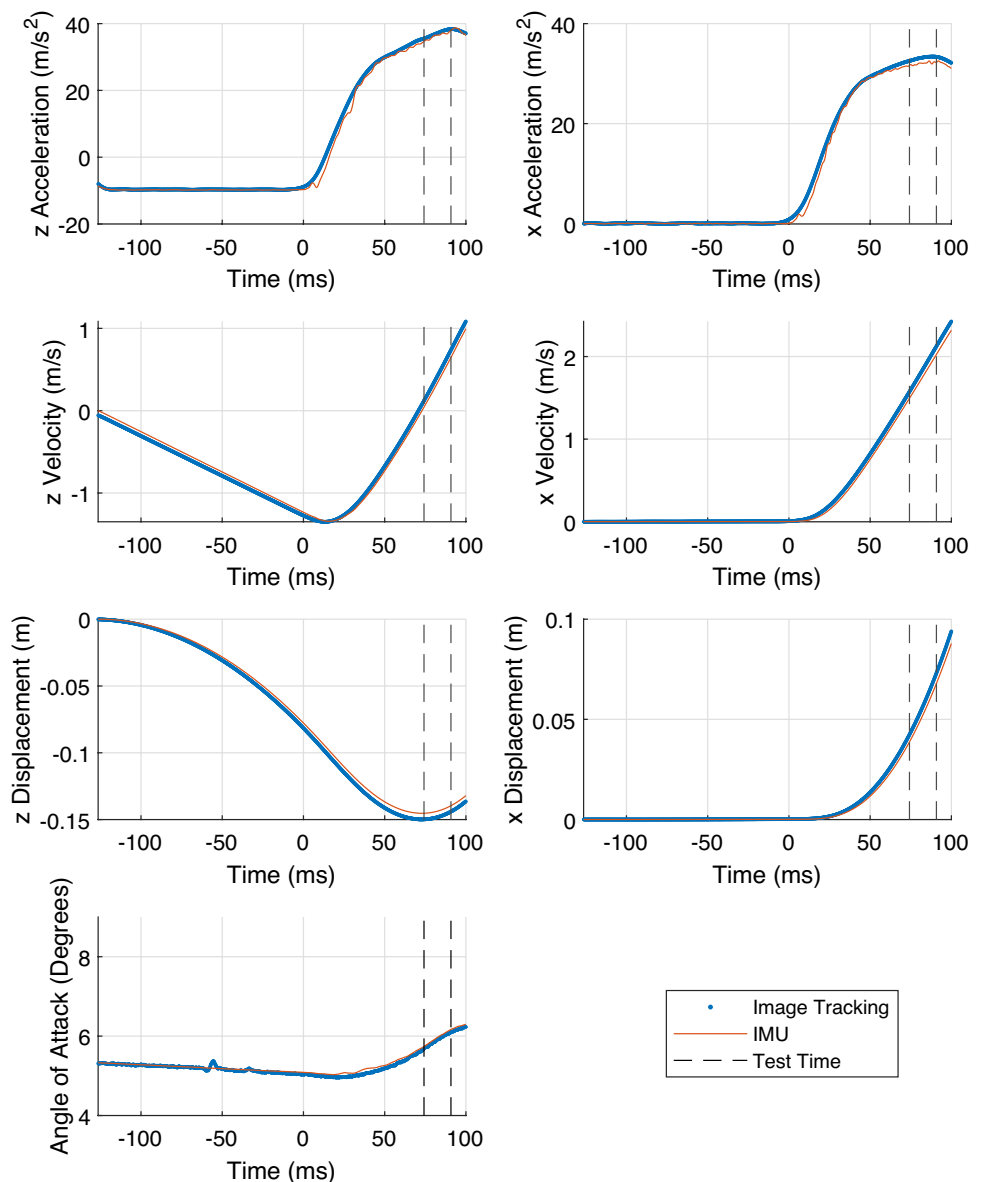


Table 3 0.7 inch force balance rated loads

Axis	Rated loading
Axial force	60 N
Normal force	360 N
Side force	360 N
Pitching moment	10.16 Nm

are shown in Table 3. The sensing strain elements are at the end of a supporting sting structure and arranged as a double bending beam balance type design (Ewald 2000). The main advantage of this setup is that the balance body is fabricated from a single piece of material which helps to avoid any hysteresis caused by screws or joints in the structure.

The principle of the bending beam balance is demonstrated by Fig. 7. The model is represented by the shell surrounding the sensing elements and the mounting sting is represented by the earth symbol. The strain gauges of interest for the force or moment represented are shown in red and relevant strain diagrams are also given. The forces and moments are measured relative to a reference centre which is located in the centre of the beam and is 46 mm from the tip of the balance for the 0.7 inch balance used in these experiments.

The principle of measuring normal (F_z) or side (F_y) forces for these balances is identical. Upon application of a pure normal force (shown on the left in Fig. 7), bending strains of equal magnitude but opposite sign are imparted at the strain gauge locations. Therefore subtraction of the

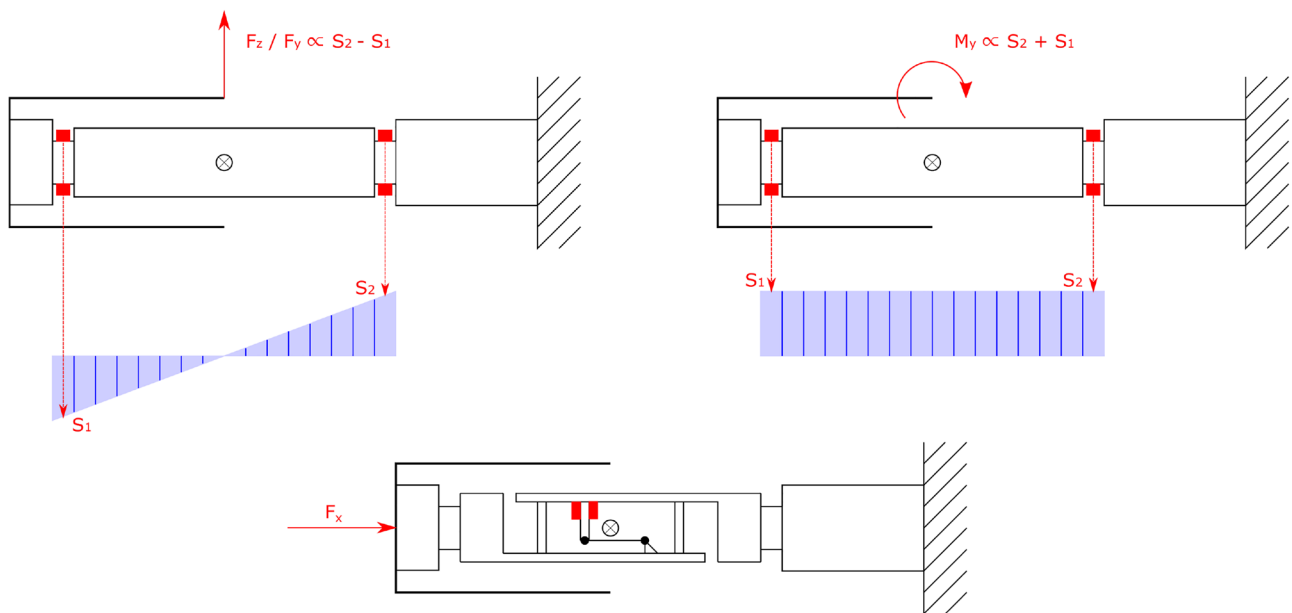


Fig. 7 Principle of beam bending force balance operation (adapted from Ewald 2000). The shell represents the model, earth symbol the sting and red elements strain gauges of interest. Shear stress diagrams are shown for the normal and pure moment loading cases

strains results in a signal proportional to the normal force. The right-hand side of Fig. 7 shows the balance response to a loading case of pure pitching moment. This results in a constant bending strain along the beam; and therefore, the addition of the stresses at the strain gauge position results in a signal proportional to the pitching moment.

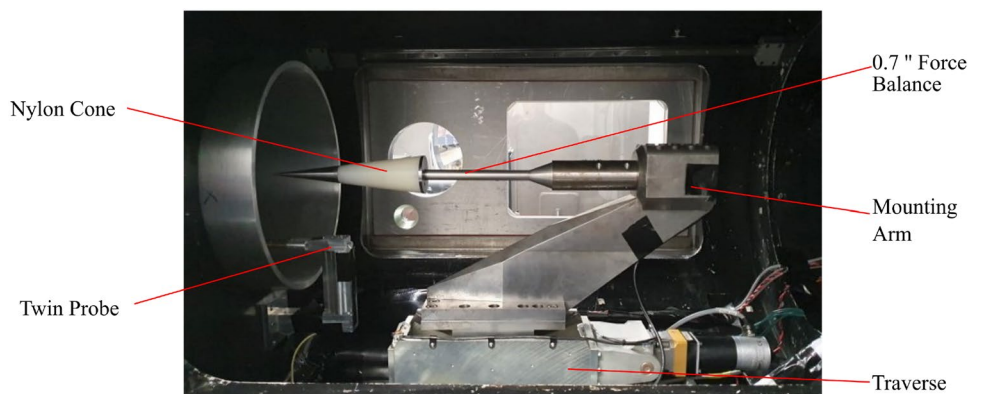
The measurement of axial force component in these balances is more complex. There are two reasons for this; firstly it is typical for aerodynamic tests with slender bodies that the axial force is of much lower magnitude than the other force components. Secondly, this force results in only longitudinal stresses in the beam which are much smaller than the bending stresses. To compensate for these two factors, an incline cut is made in the balance that separates the model side to the sting fixed part as shown at the bottom of Fig. 7. The two parts are connected by four parallelogram flexures

that allow the balance parts to move against each other in the axial direction. The movement is transferred to the force sensing flexure which is equipped with strain gauges. Ultimately this setup transforms the axial force into bending stresses that can be measured with high sensitivity.

4.2 Infrastructure

The infrastructure used to conduct force balance experiments in the Oxford HDT is shown in Fig. 8. As seen in the figure, the force balance is supported using a model mounting arm which is designed to provide minimal flow interference with the model. Dowel pins were used to connect the model to the mounting setup ensuring that the force balance strain gauges are aligned to the free-stream in roll. The mounting arm is

Fig. 8 Force balance infrastructure in the Oxford HDT



connected to a two degrees-of-freedom traverse that allows the user to set pitch between $\pm 15^\circ$ and yaw between $\pm 5^\circ$.

Mounted to the wall of the test section was a twin probe that is inserted near the base of the nozzle. The twin probe contained an aspirated thermocouple (Hermann et al. 2019) and a pitot pressure probe to allow for full characterisation of the free-stream flow. Schlieren imagery was used during testing to confirm that the bow shock from the probe did not impinge on the model and influence the measured forces.

4.3 Cone model

For the force balance work, two 7° half-angle conical models were used that could be easily interchanged. The first utilises the same model as for the free-flight experiments (Sect. 3.2) by exchanging the rear piece for a mounting adapter. Whilst this model was not optimised for force measurements due to its hollow nature, it could be instrumented with 6 Honeywell pressure transducers (4 radially at 90° intervals and 2 in the base) embedded on a single PCB board at the base of the model to allow for alignment with the free-stream flow and measurement of base pressure. The sensors were connected to the pressure tapings using 0.5 mm inner diameter flexible tube. A Molex PicoBlade connector was inserted into the base of the model to transfer data from the boards to an external DAQ. A thread at the front of the model allowed for different nose bluntnesses to be tested. The steel cone model is shown in exploded view in Fig. 9.

The second model, seen in Fig. 8, was a nylon cone of the same dimensions as the steel cone and can be attached to the same base plate. Unlike the steel model, the nylon model was solid apart from a bore in which the force balance can be inserted into. A solid model reduces the time it takes for the internal vibrations to damp down when the model is excited with an impulse. At the bottom of the bore, a copper crush washer is used to connect the live end of the force balance with the model. All contact surfaces were also greased. These improved connections allow for the stress waves to propagate through boundaries with

reduced reflections between the contact surfaces, reducing the interference of reflected waves. Furthermore, as presented in Sanderson and Simmons (1991), nylon exhibits greater damping of internal vibrations than steel (more energy absorbed per cycle) which results in a much faster time constant for decay in vibrational amplitude. In the context of wind tunnel experiments, vibrations within the model dampen faster during the test time, providing a high quality force signal.

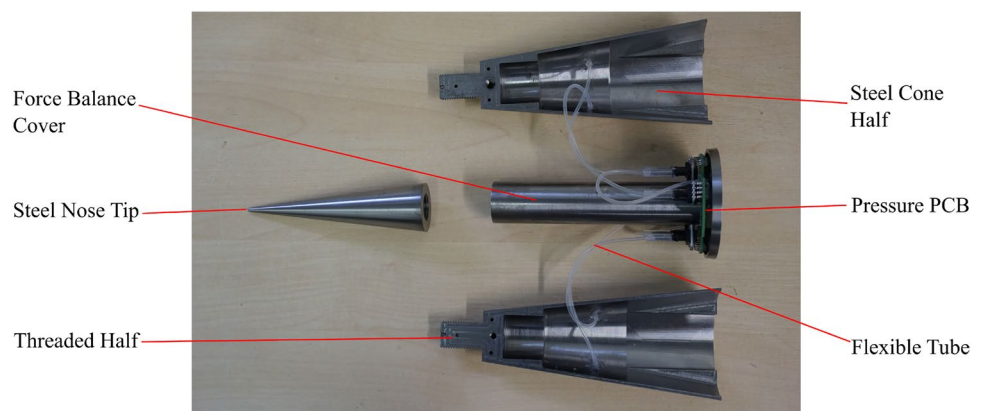
Figure 10 shows the pressure traces from a test with the model aligned to the free-stream. The four radial pressure transducers measure equal static pressure, showing that the cone is aligned. The base pressure shows a degree of transience over the first 100 ms of time post the facility firing which is due to the establishment of flow over the base of the cone. It takes approximately 50 ms for the expansion fan over the base of the cone to fully establish and begin to equalise the base pressure. The static pressures seen in Fig. 10 are not representative of the flow in Table 1 as alignment was conducted at a lower total pressure so that the vibrations of the steel model did not damage the force balance.

4.4 Data reduction

There are two ways of obtaining force data from the balance which is dependent on the method of calibration. The first method is using a static calibration and the second is a dynamic calibration using an impulse hammer. Regardless of the calibration used, the resultant forces can be resolved into orthogonal lift and drag components that can then be used to determine their corresponding aerodynamic coefficients (where L , D and M are lift force, drag force and pitching moment, respectively):

$$C_L = \frac{L}{qS}, \quad C_D = \frac{D}{qS}, \quad C_M = \frac{M}{qSc} \quad (4)$$

Fig. 9 Steel cone used for alignment in force balance experiments



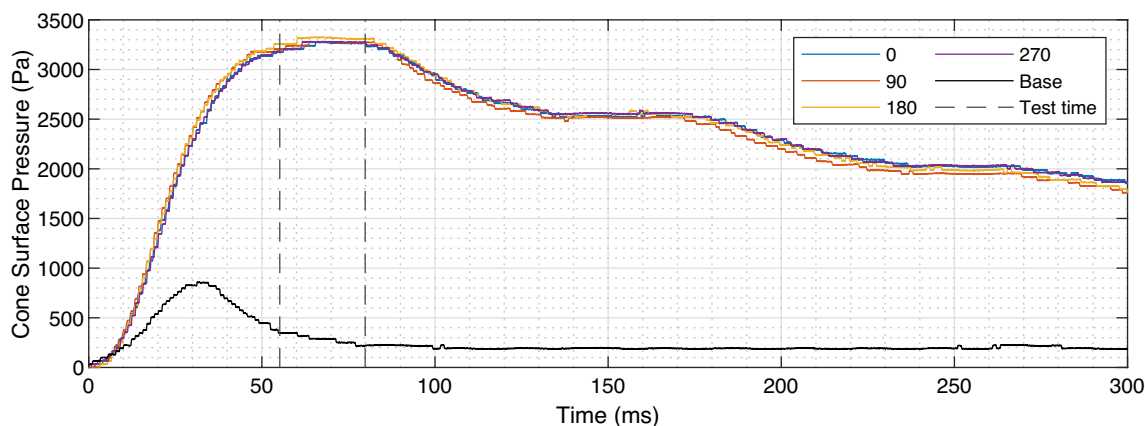


Fig. 10 Cone surface pressures for the steel model aligned with the free-stream

4.4.1 Static calibration

For an ideal multi-axis force balance, the application of a load that is purely a single component aligned with one of the measurement axis will result in a single voltage signal from the associated strain gauge. However, due to the complexity of the systems, often off-axis voltage signals will also be measured - a phenomena known as cross-coupling. The conversion of measured voltage strains to forces for the 0.7 inch load cell is given by (where V is the strain gauge voltage, k is the cross-coupling factor and F is the applied force):

$$\begin{bmatrix} V_x \\ V_y \\ V_z \\ V_{My} \end{bmatrix} = \begin{bmatrix} k_{x,x} & k_{x,y} & k_{x,z} & k_{x,My} \\ k_{y,x} & k_{y,y} & k_{y,z} & k_{y,My} \\ k_{z,x} & k_{z,y} & k_{z,z} & k_{z,My} \\ k_{My,x} & k_{My,y} & k_{My,z} & k_{My,My} \end{bmatrix} \begin{bmatrix} F_x \\ F_y \\ F_z \\ M_y \end{bmatrix} \quad (5)$$

The co-ordinate system for this balance is as follows; $+x$ towards the nose of the model, $+z$ towards the bottom of the model with $+y$ completing the orthogonal system. Or in matrix notation:

$$\mathbf{V} = \mathbf{KF} \quad (6)$$

For a well-designed force balance the cross-coupling coefficient matrix, \mathbf{K} , will be diagonally dominant meaning that there is minimal cross-coupling between the force balance channels. However, in practice this is often not the case and so careful calibration of the force balance is required. To statically calibrate a multi-axis force balance, known loads are applied individually to each of the orthogonal axes within the measurement range of the balance and the corresponding output is measured. The balance was statically calibrated externally by Novatech prior to the experiments. For each of the axes loaded, a row of the cross-coupling matrix, \mathbf{K} , can be determined. After determining the cross-coupling matrix from the calibrations, the matrix can be

inverted to determine the transfer function between output strain voltage and the applied forces:

$$\mathbf{F} = \mathbf{K}^{-1}\mathbf{V} \quad (7)$$

4.4.2 Dynamic calibration

During short duration experiments in hypersonic facilities, the aerodynamic forces around the model may reach quasi-steady equilibrium but the internal stress waves between the model and support structure may not achieve equilibrium in the test time. As a consequence, a static calibration method that assumes steady-state internal forces may not be a suitable technique for measuring forces. Therefore, a dynamic calibration may be more suitable methodology for obtaining steady-state aerodynamic forces.

The dynamic calibration used for this force balance is known as the stress wave force measurement technique (Doherty et al. 2015). The technique is based on the assumption that the system is casual, time-invariant and linear, and that the time-evolution of strain within the combined force balance, model, and supporting structure assembly is uniquely defined by the time-evolution of the aerodynamic load acting on the surface of the model. For a single-component system, a convolution between the applied load, $u(t)$ and a system impulse response function (IRF), $g(t)$, yields the measured strain response, $y(t)$, as follows:

$$y(t) = \int_0^t g(t - \tau)u(\tau)d\tau \quad (8)$$

The IRF is obtained through a calibration either prior or post the experiments. For discretised data, $u(t)$, $y(t)$, and $g(t)$ can be rewritten as:

$$y_r = \sum_{s=0}^r g_{r-s} u_s \delta t \tag{9}$$

where $r \in (0, 1, 2, \dots, k)$ and δt is the sampling rate. Rewriting this equation in matrix form yields:

$$\mathbf{y} = \mathbf{G}\mathbf{u}\delta t \tag{10}$$

If this analysis is generalised to a four component system, Eq. 10 becomes:

$$\begin{bmatrix} \mathbf{y}_x \\ \mathbf{y}_y \\ \mathbf{y}_z \\ \mathbf{y}_{My} \end{bmatrix} = \begin{bmatrix} G_{x,x} & G_{x,y} & G_{x,z} & G_{x,My} \\ G_{y,x} & G_{y,y} & G_{y,z} & G_{y,My} \\ G_{z,x} & G_{z,y} & G_{z,z} & G_{z,My} \\ G_{My,x} & G_{My,y} & G_{My,z} & G_{My,My} \end{bmatrix} \begin{bmatrix} \mathbf{u}_x \\ \mathbf{u}_y \\ \mathbf{u}_z \\ \mathbf{u}_{My} \end{bmatrix} \delta t \tag{11}$$

where G_{nm} is the IRF that relates output \mathbf{y}_n to input \mathbf{u}_m . The matrix containing all of the individual IRFs is known as the global impulse response function (GIRF) and can only be found through careful dynamic calibration. For an ideal force balance, the GIRF would be diagonally dominant with all values off the diagonal being null matrices, i.e. the input applied to an orthogonal axis only results in an output on the same axis. In this work, if the relative strain output of an off-axis term was less than 1% of the on-axis strain (for a unit normal load), the off-axis IRF was discounted. For this force balance, cross-coupling was only significant for the axial force upon the application of a normal force. This was applied to save computational time and reduced Eq. 11 to:

$$\begin{bmatrix} \mathbf{y}_x \\ \mathbf{y}_y \\ \mathbf{y}_z \\ \mathbf{y}_{My} \end{bmatrix} = \begin{bmatrix} G_{x,x} & 0 & G_{x,z} & 0 \\ 0 & G_{y,y} & 0 & 0 \\ 0 & 0 & G_{z,z} & 0 \\ 0 & 0 & 0 & G_{My,My} \end{bmatrix} \begin{bmatrix} \mathbf{u}_x \\ \mathbf{u}_y \\ \mathbf{u}_z \\ \mathbf{u}_{My} \end{bmatrix} \delta t \tag{12}$$

If the calibration process sufficiently characterises the GIRF, Eq. 12 can be used to find the applied aerodynamic load, \mathbf{u} , through a deconvolution process with the measured strains

(\mathbf{y}) and GIRF. For this work the deconvolution process was undertaken in MATLAB solving Eq. 12.

The calibration process to characterise the GIRF for this experiments was conducted with the model in situ within the wind tunnel prior to the experiments taking place. The calibration was achieved using an instrumented impact hammer (PCB Piezotronics 086C01) through application of impulsive forces at discrete model locations in orthogonal directions. Figure 11 shows the position of the impulse hits used to characterise the cone model, where A and N correspond to normal and axial impulses, respectively. As depicted in the figure, hits to characterise the axial force were conducted at the base at the four cardinal points and the nose. Characterisation of the normal component were conducted along the length of the cone at 3 positions equally spaced out (the same is true for the side force which is not depicted in the figure). By using multiple locations for impulse hammer hits and combining the individual IRFs, the stress wave patterns for the whole model was characterised. The IRFs for axial, normal (and side) were formed as shown in Eqs. 13–15 with weighting factors for each impulse. For axial force, the same overall weightings were given to the nose hit and the four combined cardinal base hits (noting the flip in polarity due to the direction of the hit). For normal and side force, equal weighting was given along the length of the cone and for the pitching moment, the two normal impulses at the extremity of the cone were combined to form the IRF.

$$G_{x,x} = \frac{1}{2}(G_{A_{nose}} - \frac{1}{4}(G_{A_N} + G_{A_W} + G_{A_E} + G_{A_S})) \tag{13}$$

$$G_{z,z} = \frac{1}{3}(G_{N_A} + G_{N_B} + G_{N_C}) \tag{14}$$

$$G_{My,My} = \frac{1}{2}(G_{N_A} - G_{N_C}) \tag{15}$$

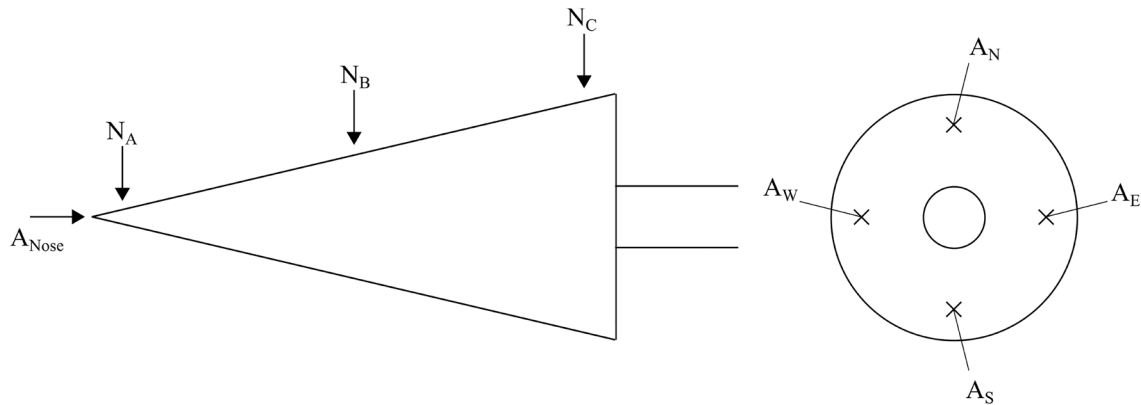


Fig. 11 Location of axial and normal impulse hits used to generate the GIRF

For each hammer hit location, three independent hammer hits were conducted. The first two hammer hits are used to generate a mean IRF at that location by deconvolving the impulse with the measured strains. The third is used as a validation, the mean IRF generated is deconvolved with the strain signal to see if the impulse for the third hit is recovered, thereby giving confidence that the IRF is valid and insensitive to small changes in component strains. This is completed for all hammer hit locations.

5 Results

The following section presents the experimental results for both force measurement techniques in the form of raw force signals and aerodynamic coefficients. Comparisons are made between the free-flight methodology and the force balance setup used for these experiments. It must be noted that uncertainties are specific to the University of Oxford 0.7 inch force balance and may be improved with a different force balance design.

5.1 Raw force signals

The first useful comparison to consider are the raw unfiltered force data. Ultimately, the cleaner the raw force signal, the lower the overall uncertainty in forces and hence coefficients. Figure 12 presents the measured unfiltered forces from both the force balance (static and dynamic calibration) and in free-flight at zero degrees angle of attack. The image tracking forces are not presented here as it is not a direct force measurement (displacements are measured) unlike the other methodologies. It can be seen from the static force balance data that vibrations within the model - support structure do not damp out in the test time and heavily superimpose themselves on the measured strain signals. This results in large oscillations within the force data. For steady signals to be measured, the aerodynamic forces must reach equilibrium with the resultant stresses applied to the load cells of the force balance. With application of the dynamic calibration, the magnitude of the vibrations is heavily reduced and results in a much cleaner force signal with respect to time; however, the oscillations are not completely removed.

However, the raw signal with the least oscillatory behaviour is the free-flight IMU data. By removing the rigid mount, internal vibrations decay much faster within the model and are not imposed on the IMU resulting in clean accelerations (hence forces) measured in the test time. Therefore, the free-flight technique will have the lowest statistical uncertainties when the force is averaged over the test time. This is shown in Table 4 where the standard deviation for free-flight is 1.4 % of the mean value compared to 22.1

% for the statically calibrated force balance data. The unfiltered normal force signals also exhibit oscillatory behaviour for the force balance albeit at a slower frequency. This is expected as the balance acts as a oscillating cantilever for this force measurement axis due to the sting. The IMU data for the normal axis is more oscillatory than for the drag data reflected in the higher standard deviation of the mean for this axis (in Table 4). This result is unsurprising as due to the design of the DAQ mount, it is less rigid on the normal axis than on the axial axis so oscillations do not damp out as quickly. Regardless, the standard deviation of the IMU data is still lower for all components than the force balance techniques.

5.2 Aerodynamic coefficients

For these experiments, tests were conducted using each methodology at 0, 3 and 6° angle of attack; 3 in free-flight and 5 tests with the force balance giving data for both static and dynamic calibrations. The data are compared with numerical results from a hypersonic panel method code which includes a viscous streamline correction at the Mach 5 condition. The algorithm traces streamlines across the body of a triangulated mesh of the model and uses the streamlines to calculate a local Reynolds number for each panel. The Smart-Meador method (Meador and Smart 2005) is used to calculate a reference boundary layer temperature. Skin friction is then calculated using Eckert's procedure (Eckert 1956). For more details on the panel code, see (Hyslop et al. 2022). Uncertainties presented for the free-flight and force balance data are presented as error bars on the figures and were calculated using Moffat's error propagation method (Moffat 1988) for free-stream parameters, model properties and through the force derivation. For the image tracking, the algorithm is perturbed by the displacement standard deviation discussed in Sect. 3.3.2. For all experimental data, the uncertainties are highest for the static force balance calibration and lowest for the free-flight data. The uncertainty in angle of attack, however, is higher for the free-flight as it relies on an image tracking rather than the direct measurement of free-stream alignment using pressure transducers as for the force balance.

Figure 13 shows the variation of lift coefficient with angle of attack which shows a positive linear trend with a zero degree lift coefficient value of zero, reflecting the symmetric shape of the cone. All experimental data points agree within the experimental uncertainty and are in good agreement with the numerical predictions. At 6° angles of attack, the dynamic calibration differs from the static calibration by 12.7% with the static calibration over predicting. This is likely due to the method of calibrating the force balance for the static tests as only 5 data points were taken over the range of the balance for the calibration which could result

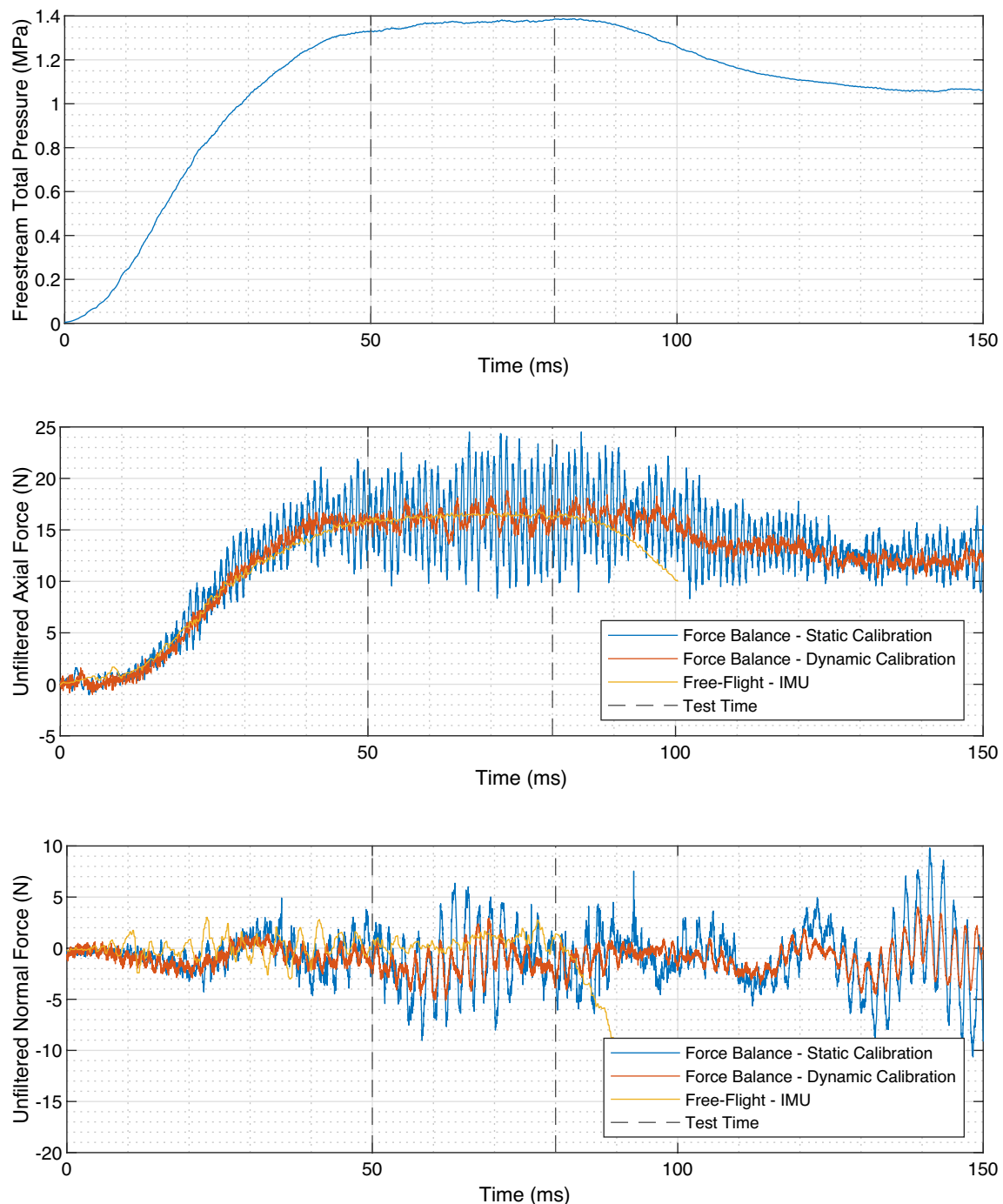


Fig. 12 Freestream total pressure (top), unfiltered axial forces (middle) and unfiltered normal force (bottom) for the different force measurement techniques at zero degree angle of attack

in error if there is some degree of nonlinearity or hysteresis in the system.

The variation of drag coefficient with angle of attack is shown in Fig. 14. For this figure, both the viscous and inviscid numerical results are plotted. The inviscid cases are not shown on the other figures as at these low angles of attack, the effects of viscosity are minimal on lift and

pitching moment. All of the data points lie slightly above the viscous numerical predictions. One reason for this could be explained in the calculation of base pressure in the panel method code. As seen in Fig. 10, the base pressure is not quite at equilibrium for the duration of the first plateau of test time which would result in an offset in drag coefficient. Whilst force balance data are acquired for all plateaus during

Table 4 Force technique statistical properties for unfiltered forces at zero Angle of attack

Technique	F_x Mean (N)	F_x std dev (N)	F_z Mean (N)	F_z std dev (N)
F.B. static	16.45	± 3.64	-1.25	± 3.15
F.B. dynamic	16.14	± 0.91	-1.22	± 1.53
Free-flight	16.30	± 0.23	0.61	± 0.68

a test, in free-flight the model is no longer in the core flow so data cannot be obtained. Lift-to-drag ratio is shown in Fig. 15 and shows good agreement with the numerical and experimental data.

Pitching moment coefficient with angle of attack is shown in Fig. 16 and is referenced from the virtual apex of the cone. The gradient of pitching moment with angle of attack is negative, as would be expected from this reference point, as it would show static stability if the CoG was hypothetically

in this location. Agreement between all methodologies lie within the uncertainties.

5.3 Comparison of methodologies

In a comparison of the methodologies, one of the most important factors to take into account are the experimental uncertainties for the techniques. The maximum uncertainties for each of the measurement axis of interest are shown in Table 5 for the different experimental methods. They are presented in the form of raw force/moment so that the uncertainties can be seen without the influence of the free-stream uncertainties as well as in coefficient form which give uncertainties for both the facility free-stream (see Table 1) and the measurement technique. For all cases, the static force balance calibration gives the highest uncertainties followed by the dynamic calibration. The uncertainties for free-flight are 50% better or more for all of the measurement axis. It is also shown that the image tracking and IMU measurements

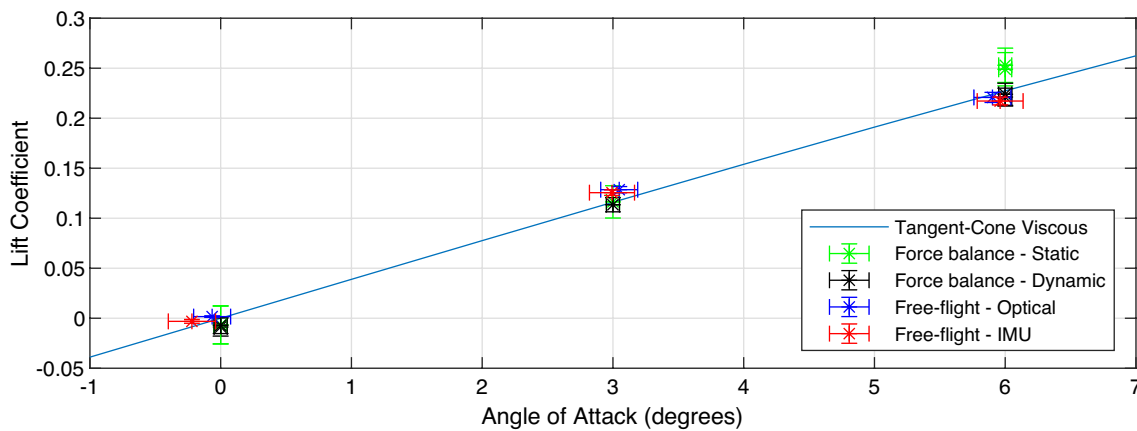


Fig. 13 Lift coefficient at Mach 5 condition. Individual tests plotted against tangent-cone numerical prediction

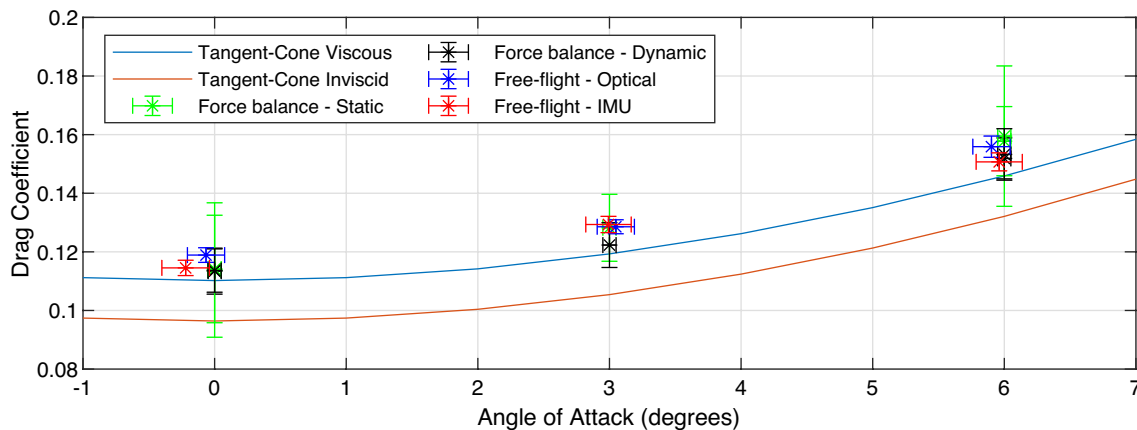


Fig. 14 Drag coefficient at Mach 5 condition. Individual tests plotted against tangent-cone numerical prediction

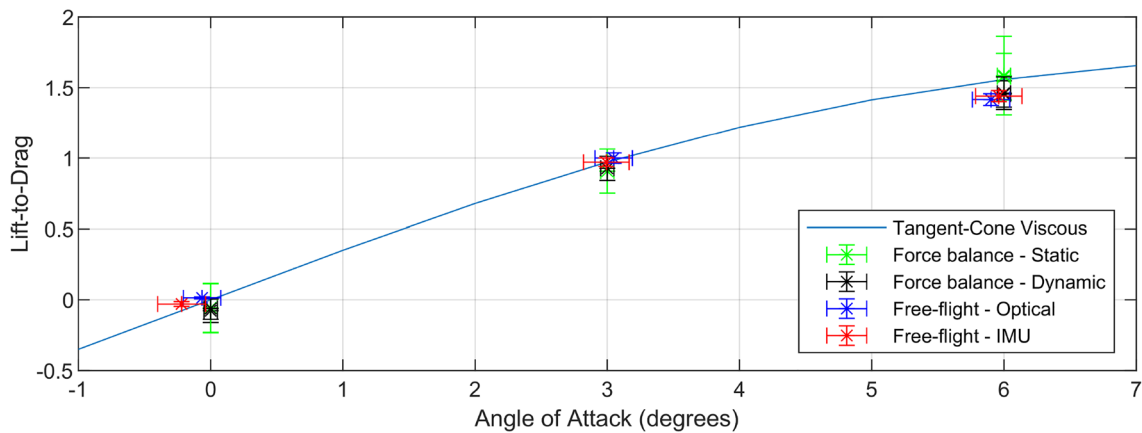


Fig. 15 Lift-to-drag ratio at Mach 5 condition. Individual tests plotted against tangent-cone numerical prediction

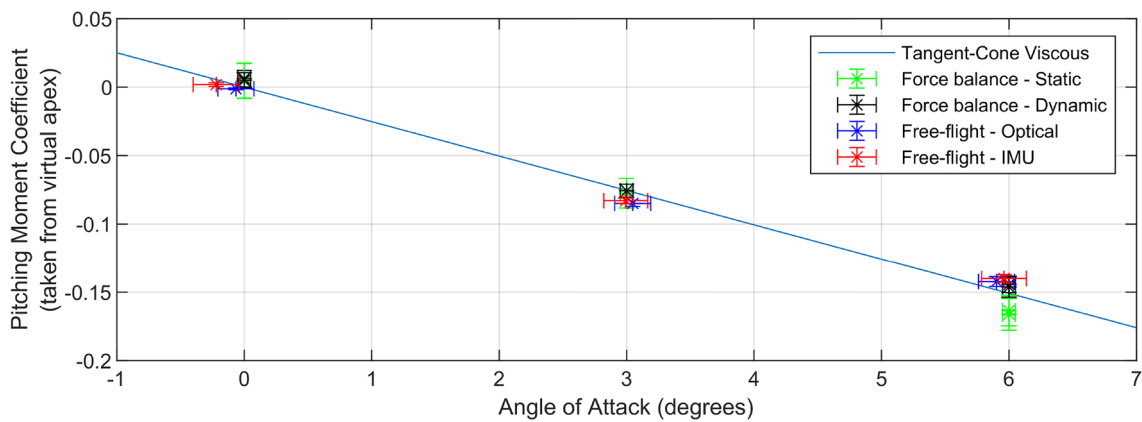


Fig. 16 Pitching moment coefficient (referenced from virtual apex of cone) at Mach 5 condition. Individual tests plotted against tangent-cone numerical prediction

Table 5 Force technique experimental uncertainties

Technique	C_L	L (N)	C_D	D (N)	C_M	M (Nm)
Force balance - <i>Static</i>	± 0.019	± 2.74	± 0.024	± 3.46	± 0.012	± 0.42
Force balance - <i>Dynamic</i>	± 0.011	± 1.59	± 0.009	± 1.27	± 0.007	± 0.27
Free-flight - <i>IMU</i>	± 0.004	± 0.56	± 0.003	± 0.44	± 0.003	± 0.10
Free-flight - <i>Optical</i>	± 0.005	± 0.73	± 0.004	± 0.53	± 0.004	± 0.13

give very similar uncertainties. A sensitivity analysis for the free-flight tests show the largest contribution to the uncertainties of the aerodynamic coefficients is the uncertainty of the measured accelerations. A shift from micro-electro-mechanical systems (MEMS) accelerometers to other forms of accelerometer may reduce these uncertainties further. For

the force balance, the main contribution to the uncertainties is from the internal vibrations of the balance.

Other factors which must be taken to account are the ease of the experiments. Once a force balance experiment is setup and aligned with the free-stream, it is very simple to adjust angle of attack on the traverse and so is quick to obtain a sweep of data with angle of attack. For free-flight, the model

must be returned to the release mechanism at the start of each test which can be time consuming if the facility test section needs to be evacuated prior to a test. Another consideration for free-flight is the greater difficulty of testing at a specific angle of attack. For these experiments, the release has a variation of $\pm 0.2^\circ$ coupled with the potential for the model to pitch if the CoG is not at CoP which can make it more challenging to achieve the desired angle of attack. This is acceptable, however, if the experimenter is interested in general trends with respect to angle of attack and the uncertainty is not an issue. Another challenge for static free-flight is that the experimenter needs a prediction of CoP location prior to experiments so that the model can be designed to be ballasted suitably for static free-flight. This becomes more of an issue with complex geometries where CFD CoP predictions become much more difficult.

That is not to say that force balances do not pose their own problems. The uncertainties are much higher in these set of experiments and they are largely driven by the internal stress waves and harmonic structural oscillations not reaching equilibrium during the experimental test time. For a force balance - model structure to be suitable for use in hypersonic facilities with a static calibration, several natural frequency cycles must pass in the test time for steady state forces to be measured (Bernstein and Pankhurst 1975). For cantilever sting based force balances, creating a natural frequency that is high enough to achieve this is very difficult; and therefore, dynamic calibration is often required. Furthermore, dynamic characterisation of complex geometries is challenging due to the lack of flat edges providing a clean surface for an impulse hammer hit. As well as these issues, combining the discrete orthogonal hammer impulses into a GIRF for a complex geometry is challenging and there is no guarantee that for a complex model the balance response is linear.

6 Conclusion

The experimental measurement of forces and moments using two independent measurement techniques have been presented at the same free-stream conditions for a 7° half-angle cone at a Mach 5 condition, providing to the authors knowledge, the first direct comparison of the two techniques in the same facility for the identical model geometries. It has been shown that all 3 methodologies (free-flight, statically calibrated force balance and dynamic-calibrated force balance) can provide accurate force and moment data but with varying uncertainties. As the force balance requires careful design of the string-model supporting structure to reduce the impact of internal vibrations from external aerodynamic forces imposing on the strain gauges, it is more susceptible to fluctuations about the mean data point than for the

unconstrained free-flight methodologies which is ultimately reflected in the higher uncertainties for force balance data (both calibrations). These uncertainties may be reduced further if the force balance is designed optimally for the model being tested by increasing the natural frequency of the system so that the oscillations decay faster. Overall, it has been shown that the uncertainties for force measurement for the free-flight technique are half as much as the force balance in the University of Oxford High Density Tunnel demonstrating that free-flight is the preferred means at achieving high-quality, low-uncertainty force measurements in short duration facilities.

Acknowledgements This research was funded and supported by DSTL. The authors would like to thank Trevor Birch (DSTL) for his technical support of the research. The authors would like to acknowledge the exhaustive work of Tristan Crumpton for operating the HDT during testing. We would also like to thank Prof. Andrew Neely and Mr Liam McQuellin from UNSW Canberra for supplying the free-flight DAQs. Further thanks go to Tamara Sopek for setting up the nozzle CFD simulations.

Author Contributions A.H. was responsible for conceptualisation, data curation, formal analysis, and writing of the main manuscript text. M.M and L.D. were responsible for supervision of the work and assisted with the interpretation of data. All authors reviewed the manuscript.

Funding Not applicable.

Availability of data and materials Data available within the manuscript.

Declarations

Ethical approval Not applicable.

Conflict of interest Not applicable.

Open Access This article is licensed under a Creative Commons Attribution 4.0 International License, which permits use, sharing, adaptation, distribution and reproduction in any medium or format, as long as you give appropriate credit to the original author(s) and the source, provide a link to the Creative Commons licence, and indicate if changes were made. The images or other third party material in this article are included in the article's Creative Commons licence, unless indicated otherwise in a credit line to the material. If material is not included in the article's Creative Commons licence and your intended use is not permitted by statutory regulation or exceeds the permitted use, you will need to obtain permission directly from the copyright holder. To view a copy of this licence, visit <http://creativecommons.org/licenses/by/4.0/>.

References

- Bernstein L, Pankhurst RC (1975) Force measurements in short-duration hypersonic facilities. Technical report
- Calloway RL (1981) Force and moment, flow-visualization, and boundary-layer tests on a shuttle orbiter model at Mach 6. Technical report
- Canny J (1986) A computational approach to edge detection. *IEEE Trans Pattern Anal Mach Intell* PAMI 8(6):679–698

- D Hillier J, Doherty L, Estruch-samper D, Barth J, Mcgilvray M (2022) HiSST: 2nd international conference on high-speed vehicle science & technology thermal effects of plume impingement on a hypersonic vehicle (September), 1–13
- Dayman Jr B (1966) Free-flight testing in high-speed wind tunnels. Technical report
- Doherty LJ, Smart MK, Mee D (2015) Measurement of three-components of force on an airframe integrated scramjet at Mach 10. In: 20th AIAA international space planes and hypersonic systems and technologies conference, p 3523
- Eckert ERG (1956) Engineering relations for heat transfer and friction in high-velocity laminar and turbulent boundary-layer flow over surfaces with constant pressure and temperature. *Trans ASME* 78(6):1273–1283
- Ewald BFR (2000) Multi-component force balances for conventional and cryogenic wind tunnels. *Meas Sci Technol* 11(6):81
- Gibbons NN, Damm KA, Jacobs PA, Gollan RJ (2023) Eilmer: an open-source multi-physics hypersonic flow solver. *Comput Phys Commun* 282:108551
- Gossir G, Puerto D, Ilich Z, Paris S, Chazot O, Rumeau S, Spel M, Annaloro J (2020) Aerodynamic characterization of space debris in the VKI Longshot hypersonic tunnel using a free-flight measurement technique. *Exp Fluids*. <https://doi.org/10.1007/s00348-020-02995-7>
- Hermann T, Mcgilvray M, Hambidge C, Doherty LJ, Buttsworth D (2019) Total temperature measurements in the oxford high density tunnel. In: FAR conference. <https://doi.org/10.2514/1.21014>
- Hough PVC (1962) Method and means for recognizing complex patterns. Google Patents
- Hyslop AM, Mcgilvray M, Doherty LJ (2022) Free-flight aerodynamic testing of a 7 degree half-angle cone. In: AIAA SCITECH 2022 Forum, p 1324
- Hyslop AM (2023) Force measurement techniques in short duration hypersonic facilities. University of Oxford, Oxford
- Hyslop A, Doherty LJ, Mcgilvray M, Neely A, McQuellin LP, Barth J, Mullen G (2021) Free-flight aerodynamic testing of the skylon space plane. *J Spacecr Rockets* 58:1487–1497
- Kennell C, Neely AJ, Buttsworth DR, Choudhury R, Tahtali M (2016) Free flight testing in hypersonic flows: HEXAFly-INT EFTV. In: 54th AIAA aerospace sciences meeting, p 1152. <https://doi.org/10.2514/6.2016-1152>
- Kennell C, Reimann B, Choudhury R, Buttsworth D, Neely A (2017) Subscale hypersonic free flight dynamics of HEXAFly-INT EFTV+ ESM (multibody separation). In: 7th European conference for aeronautics and space science
- Keyes FG (1951) A summary of viscosity and heat-conduction data for He, A, H₂, O₂, CO, CO₂, H₂O, and air. *Trans ASME* 73:589–596
- Laurence SJ, Hornung HG (2009) Image-based force and moment measurement in hypersonic facilities. *Exp Fluids* 46(2):343–353
- Leiser D, Löhle S, Zander F, Buttsworth DR, Choudhury R, Fasoulas S (2022) Analysis of reentry and break-up forces from impulse facility experiments and numerical rebuilding. *J Spacecr Rockets* 59:1276–1288
- McGilvray M, Doherty LJ, Neely AJ, Pearce R, Ireland P (2015) The Oxford high density tunnel. In: 20th AIAA international space planes and hypersonic systems and technologies conference, p 3548. <https://doi.org/10.2514/6.2015-3548>
- McQuellin LP, Kennell CM, Neely AJ, Sytsma MJ, Silvester T, Choudhury R, Buttsworth DR (2020) Investigating endo-atmospheric separation of a hypersonic flyer-sustainer using wind tunnel based free-flight. 23rd AIAA international space planes and hypersonic systems and technologies conference, 2020, pp 1–24. <https://doi.org/10.2514/6.2020-2451>
- Meador WE, Smart MK (2005) Reference enthalpy method developed from solutions of the boundary-layer equations. *AIAA J* 43(1):135–139
- Mee DJ (2003) Dynamic calibration of force balances for impulse hypersonic facilities. *Shock Waves* 12(6):443–455
- Milhaus M, Levine J, Johannesen B (1971) Space shuttle: basic hypersonic force data for Grumman delta wing orbiter configurations ROS-NB1 and ROS-WB1. Technical report
- Moffat RJ (1988) Describing the uncertainties in experimental results. *Exp Therm Fluid Sci* 1(1):3–17
- Park SH, Park G (2020) Separation process of multi-spheres in hypersonic flow. *Adv Space Res* 65(1):392–406. <https://doi.org/10.1016/j.asr.2019.10.009>
- Pick GS (1971) Sting effects in hypersonic base pressure measurements. Technical report, TR AL-85, Dec. 1971, Naval Ship Research and Development Center. Md, Bethesda, p 1971
- Sanderson SR, Simmons JM (1991) Drag balance for hypervelocity impulse facilities. *AIAA J* 29(12):2185–2191
- Stetson KF (1992) Hypersonic boundary-layer transition. In: *Advances in hypersonics*, pp 324–417
- Tanno M, Tanno H (2021) Aerodynamic characteristics of a free-flight scramjet vehicle in shock tunnel. *Exp Fluids* 62(7):1–12
- Tanno H, Komuro T, Sato K, Fujita K, Laurence SJ (2014) Free-flight measurement technique in the free-piston high-enthalpy shock tunnel. *Rev Sci Instrum* 85(4):45112
- von Gioi RG, Randall G (2017) A sub-pixel edge detector: an implementation of the canny/devernay algorithm. *IPOL J* 7:347–372
- Wuilbercq R, Pescetelli F, Minisci E, Brown RE (2014) Influence of boundary layer transition on the trajectory optimisation of a reusable launch vehicle. In: 19th AIAA international space planes and hypersonic systems and technologies conference, p 2362. <https://doi.org/10.2514/6.2014-2362>
- Wylie S, Doherty L, Mcgilvray M (2018) Commissioning of the Oxford high density tunnel (HDT) for boundary layer instability measurements at Mach 7. In: 2018 fluid dynamics conference, p 3074. <https://doi.org/10.2514/6.2018-3074>

Publisher's Note Springer Nature remains neutral with regard to jurisdictional claims in published maps and institutional affiliations.